



This is the accepted manuscript made available via CHORUS. The article has been published as:

Defect structure in quantum-cutting  $\text{Yb}^{3+}$ -doped  $\text{CsPbCl}_3$  perovskites probed by x-ray absorption and atomic pair distribution function analysis

Kyle T. Kluherz, Sebastian T. Mergelsberg, David E. Sommer, Joo Yeon D. Roh, Sarah A. Saslow, Daniel Biner, Karl W. Krämer, Scott T. Dunham, James J. De Yoreo, and Daniel R. Gamelin

Phys. Rev. Materials **6**, 074601 — Published 22 July 2022

DOI: [10.1103/PhysRevMaterials.6.074601](https://doi.org/10.1103/PhysRevMaterials.6.074601)

# Defect Structure in Quantum-Cutting Yb<sup>3+</sup>-Doped CsPbCl<sub>3</sub> Perovskites

## Probed by X-Ray Absorption and Atomic Pair Distribution Function Analysis

Kyle T. Kluherz,<sup>1</sup> Sebastian T. Mergelsberg,<sup>2</sup> David E. Sommer,<sup>3</sup> Joo Yeon D. Roh,<sup>1</sup>  
Sarah A. Saslow,<sup>2</sup> Daniel Biner,<sup>4</sup> Karl W. Krämer,<sup>4</sup> Scott T. Dunham,<sup>3</sup> James J. De Yoreo,<sup>2</sup>  
and Daniel R. Gamelin<sup>1,\*</sup>

<sup>1</sup>*Department of Chemistry, University of Washington, Seattle, WA 98195*

<sup>2</sup>*Physical Sciences Division, Pacific Northwest National Laboratory, Richland, WA 99352*

<sup>3</sup>*Department of Electrical Engineering, University of Washington, Seattle, WA, 98195*

<sup>4</sup>*Department of Chemistry, Biochemistry, and Pharmacy, University of Bern, Freiestrasse 3, CH-3012 Bern, Switzerland*

Email: gamelin@chem.washington.edu

---

**Abstract.** Ytterbium-doping in all-inorganic lead-halide perovskites (CsPb(Cl<sub>1-x</sub>Br<sub>x</sub>)<sub>3</sub>) generates novel properties including quantum cutting and narrow line emission, making these materials attractive spectral down-converters for solar photovoltaics. The relationship between this optical efficiency and the defect structure(s) associated with Yb<sup>3+</sup> dopants within perovskites is not well understood. Various charge-neutral doping motifs have previously been proposed and studied computationally, including clusters involving two substitutional Yb<sup>3+</sup> ions charge-compensated by a single local Pb<sup>2+</sup> vacancy. Near-band-edge defect states associated with such motifs are believed to play an important mechanistic role in quantum cutting itself. Here, we report the results of X-ray absorption and X-ray total-scattering measurements on ytterbium-doped CsPbCl<sub>3</sub>. XANES shows that the dopant oxidation state is exclusively Yb<sup>3+</sup>, and a combination of Yb L<sub>3</sub> and Pb L<sub>3</sub> EXAFS shows that this Yb<sup>3+</sup> substitutes exclusively at Pb<sup>2+</sup> sites, where it adopts a pseudo-octahedral [YbCl<sub>6</sub>]<sup>3-</sup> coordination environment. Shell-by-shell fits to the data show a short Yb-Cl bond distance of 2.58 Å compared to the Pb-Cl bond distance of 2.83 Å. We confirm this finding by X-ray pair distribution function analysis, which also shows evidence of additional Pb<sup>2+</sup> vacancy formation induced by Yb<sup>3+</sup> doping. We evaluate whether this is the primary mechanism of charge compensation using simulated EXAFS and pair distribution function data for several computed defect structures. Together, these results resolve the local dopant structures and charge-compensation mechanisms in lanthanide-doped all-inorganic lead-halide perovskites, and, as such, significantly advance the understanding of structure-function relationships in this important class of materials.

---

## Introduction

Lanthanide doping has been reported to increase lattice stability, expand optical properties, and improve the photovoltaic performance of lead-halide perovskites [1-5].  $\text{Yb}^{3+}$  doping into cesium-lead-halide ( $\text{CsPb}(\text{Cl}_{1-x}\text{Br}_x)_3$ ,  $0 \leq x \leq \sim 2/3$ ) perovskites can also produce photoluminescence quantum yields (PLQYs) above 100% *via* a unique quantum-cutting process, in which the energies of blue or UV photons absorbed by the perovskite are split to yield two emitted near-infrared photons from  $\text{Yb}^{3+}$  dopants [3,6-9]. Such "quantum cutting" has been demonstrated to markedly improve the power-conversion efficiencies (PCE) of silicon and copper indium gallium selenide photovoltaics [3], and it has the capacity to increase the PCEs of high-efficiency silicon heterojunction and other red-sensitive solar cells by as much as ~20% (relative) [10].

The specific ytterbium species that enable quantum cutting remain largely unknown. The  $\text{Yb}^{3+}$  emission from quantum-cutting  $\text{CsPbCl}_3$  nanocrystals, thin films, and bulk single crystals has been studied in detail [11]. These data provide evidence of multiple  $\text{Yb}^{3+}$  species coexisting in these materials, but just one primary  $\text{Yb}^{3+}$  emission center, identified as having pseudo-octahedral coordination. The  $\text{Yb}^{3+}$  speciation probed by photoluminescence (PL) is biased toward detection of only those ions participating in quantum cutting, however, and consequently reveals little about associated dopant-induced defects. Specifically,  $\text{Yb}^{3+}$  ions are believed to substitute for  $\text{Pb}^{2+}$  in the perovskite lattice, but because of their extra positive charges, such substitution requires charge compensation *via* defect formation. A charge-neutral defect cluster involving two substitutional  $\text{Yb}^{3+}$  ions ( $[\text{Yb}^{3+}]^+$ ) compensated by an adjacent  $\text{Pb}^{2+}$  vacancy ( $[\text{V}_{\text{Pb}}]^{2-}$ ) has been proposed as a candidate structure (*i.e.*,  $[\text{Yb}^{3+}\text{-V}_{\text{Pb}}\text{-Yb}^{3+}]^0$ ) [8]. Computational studies [12] support the existence of this defect cluster in doped  $\text{CsPbCl}_3$ , and also predict the coexistence of other defect motifs, most prevalently substitutional  $[\text{Yb}^{3+}]^+$  ions compensated by distal  $[\text{V}_{\text{Pb}}]^{2-}$ , and  $[\text{Yb}^{3+}\text{-V}_{\text{Pb}}]^-$  defects with distal  $[\text{Yb}^{3+}]^+$  for compensation. The speciation distribution depends on the  $\text{Yb}^{3+}$  concentration and the chemical activities of the other lattice constituents. Near-band-edge states associated with such defect motifs appear to play an important mechanistic role in quantum cutting itself [8,11,13]. PL may also overlook other relevant species. For example,  $\text{Yb}^{3+}$  is among the most easily reduced of the trivalent lanthanides, raising the possibility of yet-undetected  $\text{Yb}^{2+}$  species. Indeed,  $\text{CsYbI}_3$  perovskites with B-site  $\text{Yb}^{2+}$  are known [14], and an easily reduced  $\text{Yb}^{3+}$  site has been proposed as a

transient intermediate in some quantum-cutting mechanistic schemes [15,16]. To date, X-ray diffraction (XRD) has been inconclusive about the structural changes to CsPbCl<sub>3</sub> associated with lanthanide doping, with some reports showing no changes in diffraction until doping exceeds ~10% (percentage of total B-site cations) [7,8,11], and others showing small peak shifts and new peaks at only ~1% doping [6,17]. Further structural characterization is needed.

Several reports have described the use of X-ray absorption techniques to study the local structures of dopants in metal-halide perovskites, including Mn<sup>2+</sup>, Cu<sup>2+</sup>, Ni<sup>2+</sup>, and Yb<sup>3+</sup> [18-21]. Although the long-range order (*i.e.*, periodicity) of the lattice is generally not altered upon doping, the short-range order around the dopant frequently differs from that of the host lattice. For example, Ni<sup>2+</sup> and Cu<sup>2+</sup> impurities increase short-range order in metal-halide perovskites, whereas Yb<sup>3+</sup> is reported to decrease the short-range order [18,19,21]. The accompanying Pb L<sub>3</sub> EXAFS data are largely insensitive to such dopant-induced changes in short-range order. An EXAFS study of Yb<sup>3+</sup>:CsPbCl<sub>3</sub> nanocrystals supports the proposed substitution of Yb<sup>3+</sup> at Pb<sup>2+</sup> sites [19], and reports that increased doping causes an increase in anomalous band-edge emission, which the authors attributed to structural defects. Previous work has also investigated the CsPbBr<sub>3</sub> perovskite lattice *via* X-ray total scattering [22,23], identifying short- to medium-range order and domain twinning. To date, there have been no X-ray total scattering studies of doped CsPbX<sub>3</sub> perovskites. Such experiments, in conjunction with X-ray absorption spectroscopy, are anticipated to advance our understanding of the microscopic structures of these important opto-electronic materials.

Here, we report structural studies of 0.0%, 0.9% and 7.4% ytterbium-doped CsPbCl<sub>3</sub> using extended X-ray absorption fine structure (EXAFS) and pair distribution function (PDF) methods. These structural data are complemented by density functional theory (DFT) and *ab initio* molecular dynamics (AIMD) calculations. We find conclusive evidence for substitution of Yb<sup>3+</sup> at Pb<sup>2+</sup> sites in CsPbCl<sub>3</sub>, with no detectable Yb<sup>2+</sup>, and additionally observe the formation of Pb<sup>2+</sup> vacancies upon doping with Yb<sup>3+</sup>. These experimental results are discussed in relation to various proposed local defect structures.

## Methods

**Materials and Sample Preparation.** Yb<sup>3+</sup>:CsPbCl<sub>3</sub> single crystals were grown via the Bridgman technique from melts of stoichiometric admixtures of precursors (see Roh *et al* [11])

for details). For the experiments detailed here, three such samples were used; they were obtained using nominal  $\text{Yb}^{3+}$  concentrations of 0, 2, and 10% during growth, respectively, where  $\text{Yb}^{3+}$  concentrations are reported as the percentage of total *B*-site cations, *i.e.*,  $\% \text{Yb}^{3+} = 100\% * [\text{Yb}] / ([\text{Yb}] + [\text{Pb}])$ . These doping levels were selected to allow comparison across a broad range of compositions relevant to prior PL studies, while still providing good experimental signal-to-noise. Optical spectroscopy of these single crystals has been reported previously [11].  $\text{Yb}^{3+}$  contents in these crystals were determined analytically *via* ICP-AES (PerkinElmer 8300) and found to be 0.0, 0.9, and 7.4%  $\text{Yb}^{3+}$ , respectively. For ICP-AES measurements, portions of the three crystals were digested in concentrated nitric acid with sonication, then diluted with nanopure water. For XRD and PDF measurements, portions of the Bridgman crystals were gently crushed under nitrogen atmosphere with mortar and pestle to produce microcrystalline powders. Powder XRD data (Figure S1 in the Supplemental Material [24]) were collected using a Bruker D8 Discover with a Cu  $K\alpha$  source (50 kV, 1 mA). Thin film samples for X-ray absorption spectroscopy (XAS) measurements were made by single-source vapor deposition on quartz substrates followed by thermal annealing in ambient atmosphere at 250 °C for 10 min [25]. A nominal  $\text{Yb}^{3+}$  content of 5% was used, and prior work has demonstrated that the thin films contain almost the same concentration of  $\text{Yb}^{3+}$  as the single-source precursor (*e.g.*, 4.7% vs 5.0% in [25]).

**XAS Measurements.** X-ray Absorption Near Edge Structure (XANES) and Extended X-ray Absorption Fine Structure (EXAFS) spectra were collected at beamlines 20-ID-B and 9-BM at the Advanced Photon Source at Argonne National Laboratory. Yb  $L_3$  edge (8944 eV) and Pb  $L_3$  edge (13035 eV) data were collected in fluorescence mode for single crystals of each sample at room temperature under helium atmosphere with active purging (see Figure S2 in the Supplemental Material [24]). A Si(111) double-crystal monochromator was used to select the incident energy with He filled ion chambers to monitor the flux. The monochromator was calibrated using Cu foil (8979 eV) or Pb foil. The pre-edge region was collected from 200 eV to 30 eV below the edge with a step size of 5 eV and a collection time of 0.5 s at each step. From 30 eV below the edge to 30 eV above the edge, data was collected in 0.50 eV steps for 0.5 s at each step. Post-edge data was collected to 14 keV (for Yb) or 13 keV (for Pb) and obtained with a 0.05 keV step size and a collection time of 0.5 s per step. Ytterbium (II) iodide and ytterbium (III) chloride hexahydrate Yb  $L_3$  edges were collected in transmission mode for use as XANES

fitting standards. Data normalization, energy calibration, and linear-combination fitting (LCF) were performed using ATHENA software [26]. Yb XANES spectra were fit using a linear combination of spectra of the two Yb standards. R-space EXAFS data were corrected in Artemis using a Cl single scattering path from the CsPbCl<sub>3</sub> host lattice structure. For sake of clarity, we use  $R + \Delta R$  to denote the corrected radial distance axis in the EXAFS data. Simulated EXAFS data were calculated from AIMD simulated structures (*vide infra*) using the FEFF10 package [27-29]. Fits to the EXAFS data from proposed defect structures were performed with ARTEMIS software [26].

**PDF Measurements.** X-ray total scattering data were collected at beamline 11-ID-B at the Advanced Photon Source at Argonne National Laboratory [30]. Powdered single-crystal samples were measured at room temperature under a low-O<sub>2</sub> nitrogen atmosphere using monochromatic X-rays at  $\sim 86.7$  keV ( $\lambda = 0.1430$  Å). Using a Varex 4343CT area detector (150 x 150  $\mu\text{m}^2$  pixel size), the sample-to-detector distance and detector non-orthogonality were calibrated with a CeO<sub>2</sub> standard (NIST 674a). X-ray total scattering data were integrated using the GSAS-II software [31] and a radial bin size of 1400. Background subtraction and PDF processing were initially performed using the PDFgetX3 software [32], with additional quantitative processing in PDFgetX2 [33]. Raw intensity ( $I(Q)$ ) data were not rescaled in any way before analysis. For PDF processing, a  $Q_{\text{max}}$  of  $24 \text{ \AA}^{-1}$  and  $r_{\text{max}}$  of  $30 \text{ \AA}$  were used. Additional corrections account for composition (as determined by ICP), sample absorption, and Compton scattering. The PDFgui [34] package was used to determine the instrument parameters  $q_{\text{damp}} = 0.0364 \text{ \AA}^{-1}$  and  $q_{\text{broad}} = 0.00118 \text{ \AA}^{-1}$ . Partial PDFs of CsPbCl<sub>3</sub> were calculated using a reference CsPbCl<sub>3</sub> Pnma structure (ICSD #243734) [35] and the refined instrumental parameters. Differential PDFs (dPDF),  $D(r)$ , were obtained by subtracting the CsPbCl<sub>3</sub>  $G(r)$  from the data for each of the two doped Yb<sup>3+</sup>:CsPbCl<sub>3</sub> samples. For clarity,  $r$  in Å is used to denote the absolute radial distance axis in our PDF figures. The synthetic  $G(r)$  profiles were calculated from 1 ps AIMD trajectories for each model defect structure using the powder method in the Discus [36] software package, with the refined instrument parameters  $q_{\text{damp}}$  and  $q_{\text{broad}}$ . Profiles were scaled to account for differences in Yb<sup>3+</sup> concentration. Calculated profiles were computed for every 60 fs of simulation time (using 2 fs time steps) and averaged to account for thermal motion of the system over 1 ps. The first and second halves of the trajectory were compared to account for possible sampling bias, but none was found (Fig. S10). dPDF data for the simulations was

calculated by subtracting the synthetic PDF for CsPbCl<sub>3</sub> from the synthetic PDF for the respective proposed dopant structure.

**Ab Initio Simulations.** Details of the simulation methods were previously reported [12]. All first-principles calculations were carried out using the Vienna Ab-Initio Simulation Package (VASP) [37,38]. Plane-wave, Kohn-Sham density functional theory calculations employed the all-electron projector-augmented wave (PAW) method in the generalized gradient approximation (GGA) with the semilocal PBEsol functional [39-41]. In the pseudopotentials, 9 electrons of atomic Cs ( $5s^25p^66s^1$ ), 4 electrons of atomic Pb ( $6s^26p^2$ ), and 7 electrons of atomic Cl ( $3s^23p^5$ ) were treated as valence electrons, while 13 *f* electrons in the [Xe]4*f*<sup>14</sup>6*s*<sup>2</sup> valence configuration of atomic Yb were treated as frozen core states. A plane-wave basis cutoff was set to 400 eV, and a Gamma-centered *k*-point mesh was used for Brillouin-zone integration [42]. The volume, shape, and atomic positions were relaxed until interatomic Hellmann-Feynman forces were less than 0.01 eV/Å. A dopant concentration of 2.8% was used for these calculations.

AIMD simulations were run with VASP for 1 ps durations with 2 fs time steps for each defect structure. Using the Nose-Hoover thermostat and NVT ensemble, the temperature was set to 300 K, and the simulation volume was fixed to the relaxed volume of the defect supercells. All defect calculations were performed on 3x3x2 supercells derived from the 20-atom unit cell in the low-energy Pnma perovskite phase. A dopant concentration of ~7.4% was used for these simulations.

## Results and Discussion

**XANES and EXAFS Measurements.** Figure 1 shows Yb L<sub>3</sub>-edge XANES data collected for 0.9% and 7.4% Yb-doped CsPbCl<sub>3</sub> single crystals, a 5% Yb-doped CsPbCl<sub>3</sub> thin film, an ytterbium (III) chloride standard, and an ytterbium (II) iodide standard. The thin-film sample was included to assess the influence of surfaces and grain boundaries on the oxidation state of Yb. There are no significant differences between the single-crystal and thin-film data, from which we conclude that surfaces and grain boundaries do not affect the Yb oxidation state in any significant way. The Yb L<sub>3</sub> edges of the doped CsPbCl<sub>3</sub> samples agree very well with the Yb(III) standard (vertical dashed line). Fitting the 7.4% data to linear combinations of the two Yb standards allows the conclusion that 99±1% of the Yb dopants are in the Yb(III) oxidation state. The spectrum's second second-derivative (not shown) shows no evidence of any Yb<sup>2+</sup> peak,

consistent with the above conclusion. We therefore henceforth refer to these samples as  $\text{Yb}^{3+}:\text{CsPbCl}_3$ .

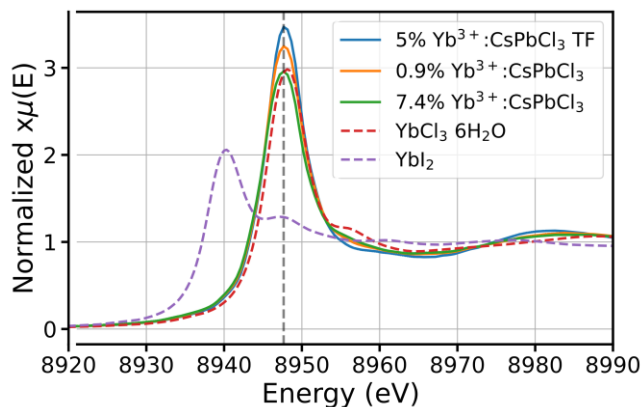


**Figure 1.** Yb  $L_3$ -edge XANES spectra for single-crystal and thin-film (TF) samples of  $\text{Yb}^{3+}:\text{CsPbCl}_3$ , compared with  $\text{Yb}^{3+}$  ( $\text{YbCl}_3 \cdot 6\text{H}_2\text{O}$ ) and  $\text{Yb}^{2+}$  ( $\text{YbI}_2$ ) standards. All  $\text{Yb}^{3+}:\text{CsPbCl}_3$  samples show the same dominant peak coinciding with the  $\text{Yb}^{3+}$  standard peak (vertical dashed line). The second derivatives of the  $\text{Yb}^{3+}:\text{CsPbCl}_3$  spectra (not shown) also show no detectable  $\text{Yb}^{2+}$ .

To probe the local structure of  $\text{Yb}^{3+}$  in the  $\text{CsPbCl}_3$  host lattice, Pb  $L_3$ -edge (13035 eV) and Yb  $L_3$ -edge (8943 eV) EXAFS data were collected for the  $\text{CsPbCl}_3$ , 0.9%  $\text{Yb}^{3+}$ , and 7.4%  $\text{Yb}^{3+}$ -doped  $\text{CsPbCl}_3$  single crystals (Figure S3, Supplemental Material [24]). Figure 2 shows the scaled, phase-corrected Fourier transform EXAFS data for the Pb  $L_3$  and Yb  $L_3$  edges of the 0.9% and 7.4%  $\text{Yb}^{3+}$ -doped  $\text{CsPbCl}_3$  single crystals. For ease of comparison, the Pb data for each sample have been scaled so their peak intensity matches that of the corresponding Yb data, but the Yb  $L_3$  edge data have not been scaled. Only the nearest-neighbor peak, corresponding to Cl single scatterers, is visible in each Pb  $L_3$  measurement, as previously reported for Pb edge data from other perovskite samples [18,19,21,43]. The Yb  $L_3$  data are similar to the Pb  $L_3$  data except that they show a marked decrease in  $R$  by  $\sim 0.2 \text{ \AA}$ , consistent with shorter  $\text{Yb}^{3+}-\text{Cl}^-$  bond lengths compared to  $\text{Pb}^{2+}-\text{Cl}^-$  bond lengths. Shell-by-shell fitting of these data shows good agreement with a structure involving 6 nearest-neighbor  $\text{Cl}^-$  anions in an octahedral arrangement around  $\text{Yb}^{3+}$ . For the data from the 7.4%  $\text{Yb}^{3+}$  sample, the shoulder at  $\sim 2.0 \text{ \AA}$  is accounted for well by the Cl single scattering path fits. We attribute the greater shoulder at  $\sim 2.1 \text{ \AA}$  in the 0.9%  $\text{Yb}^{3+}:\text{CsPbCl}_3$  Yb  $L_3$  data to Fourier noise, visible in the  $k$ -space data (see Figure S3, Supplemental Material [24]).



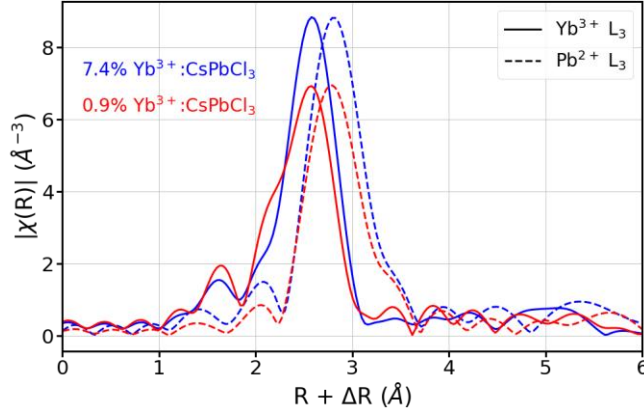


**Figure 2.** Fourier transform (real space) EXAFS spectra from the Yb  $L_3$  (solid) and Pb  $L_3$  (dashed) edges for 7.4%- (blue) and 0.9%-doped (red)  $\text{Yb}^{3+}:\text{CsPbCl}_3$  single crystals. The Pb data have been vertically scaled so the primary peak intensity matches that of the Yb  $L_3$  data for the same sample for comparison. Data have been phase-corrected to the primary peak for each edge, based on M-Cl single scattering paths, where M = Yb or Pb. A window of 1.0 to 2.8 Å was used for shell-by-shell fitting. The peak positions indicate a 0.2 Å contraction of  $[\text{YbCl}_6]^{3-}$  octahedra relative to  $[\text{PbCl}_6]^{4-}$  octahedra.

The DFT-optimized defect structures previously identified by Sommer *et al.* [12] were enlisted to assist further assessment the  $\text{Yb}^{3+}$ -related structures on an atomic scale. Figure 3 shows schematic representations of the four main defect structures considered in this work. In each structure,  $\text{Yb}^{3+}$  dopants occupy  $\text{Pb}^{2+}$  sites ( $\text{Yb}_{\text{Pb}}$ ) in the  $\text{CsPbCl}_3$  lattice. The simplest structure is a substitutional  $\text{Yb}^{3+}$  ion with no other proximal defects, *i.e.*, a  $[\text{Yb}_{\text{Pb}}]^+$  defect. This defect lacks local charge compensation and is predicted to be less prevalent than charge-compensated defect structures, particularly at experimentally relevant  $\text{Yb}^{3+}$  concentrations [12]. Among the more prevalent structures are  $\text{Yb}_{\text{Pb}}$  with an adjacent  $\text{Pb}^{2+}$  vacancy ( $\text{V}_{\text{Pb}}$ ), *i.e.*, a  $[\text{Yb}_{\text{Pb}}-\text{V}_{\text{Pb}}]^-$  defect (in conjunction with a distal  $[\text{Yb}_{\text{Pb}}]^+$ ), and charge-neutral defect clusters involving 2  $\text{Yb}_{\text{Pb}}$  ions adjacent to a single  $\text{V}_{\text{Pb}}$ , *i.e.*, a  $[\text{Yb}_{\text{Pb}}-\text{V}_{\text{Pb}}-\text{Yb}_{\text{Pb}}]^0$  "dimer" defect. Two such dimer defect structures are possible, one in a linear arrangement and the other in a bent (orthogonal) arrangement. Such structures may also exist with different orientations relative to the crystallographic axes. DFT calculations predict the energies of these various arrangements to be essentially equivalent [12]. Using these DFT structures, we performed shell-by-shell fits to the Yb EXAFS data using the Artemis package (Figure S5, Tables SI and SII in Supplemental Material [24]). All defect structures fit to the nearest-neighbor Yb-Cl scattering path equally well, with the exception of the  $[\text{Yb}_{\text{Pb}}]^+$  structure, which yields slightly higher R-factors and  $\chi^2_{\text{red}}$  goodness-of-fit values, indicating a poorer fit.

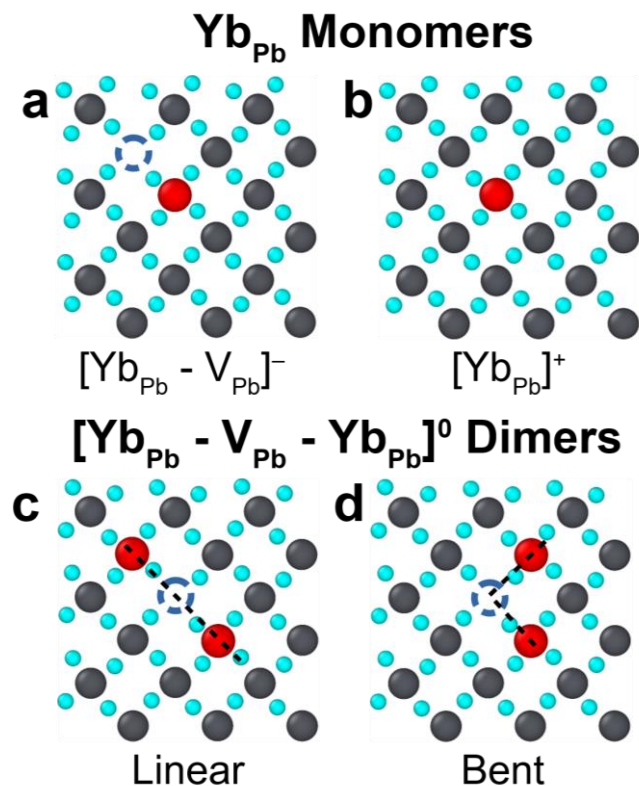


**Figure 3.** Yb<sup>3+</sup> dopant/defect CsPbCl<sub>3</sub> structures (sliced along [110] plane) used in DFT calculations. Red: Yb<sup>3+</sup>; Gray: Pb<sup>2+</sup>; Blue: Cl<sup>-</sup>. Cs<sup>+</sup> ions have been omitted for clarity. **(a)** [Yb<sub>Pb</sub>-V<sub>Pb</sub>]<sup>-</sup>: A substitutional Yb<sup>3+</sup> adjacent to a Pb<sup>2+</sup> vacancy. **(b)** [Yb<sub>Pb</sub>]<sup>+</sup>: A single substitutional Yb<sup>3+</sup>. **(c,d)** [Yb<sub>Pb</sub>-V<sub>Pb</sub>-Yb<sub>Pb</sub>]<sup>0</sup>: Charge-neutral "dimer" structures involving two substitutional Yb<sup>3+</sup> ions adjacent to a single Pb<sup>2+</sup> vacancy in (c) a linear arrangement and (d) a bent or orthogonal arrangement.

Figure 4 shows simulated EXAFS results for each of the computed Yb<sup>3+</sup> defect structures, in comparison with the experimental Yb L<sub>3</sub> EXAFS data. These data are plotted in both *k*-space and R-space. The computed *k*-space EXAFS data show only small variations in peak shape and position among the various proposed structures, with minor variations around 4, 8, and 9 Å and growing more distinct at 10 Å and beyond. The *k*-space plot terminates at 11 Å, reflecting the cutoff used in data processing. Similarly, the R-space features are quite similar for each of the 4 computed defect structures, all showing a dominant nearest-neighbor chloride peak at ~2.2 Å and only small secondary features. The vertical dashed lines in Figure 4b highlight the distances at which the most distinctive differences between computed structures are found. Unfortunately, the differences in the experimental data among these structures in either *k*- or R-space representations are too slight to enable differentiation between the defect models. Using Athena, the experimental spectra were fit using a linear combination of simulated spectra for

each structure. This exercise (not shown) found similar goodness of fit regardless of the simulated structure, likely due to structural similarities particularly in the nearest-neighbor peak, but also extending to the region where second-nearest neighboring peaks are resolved. EXAFS was thus unable to distinguish among these  $\text{Yb}^{3+}$  defect structures, and did not yield additional structural insights beyond the nearest-neighbor distances deduced from Figure 2. We therefore turned to PDF measurements to probe differences in the short-range order on the bulk scale.

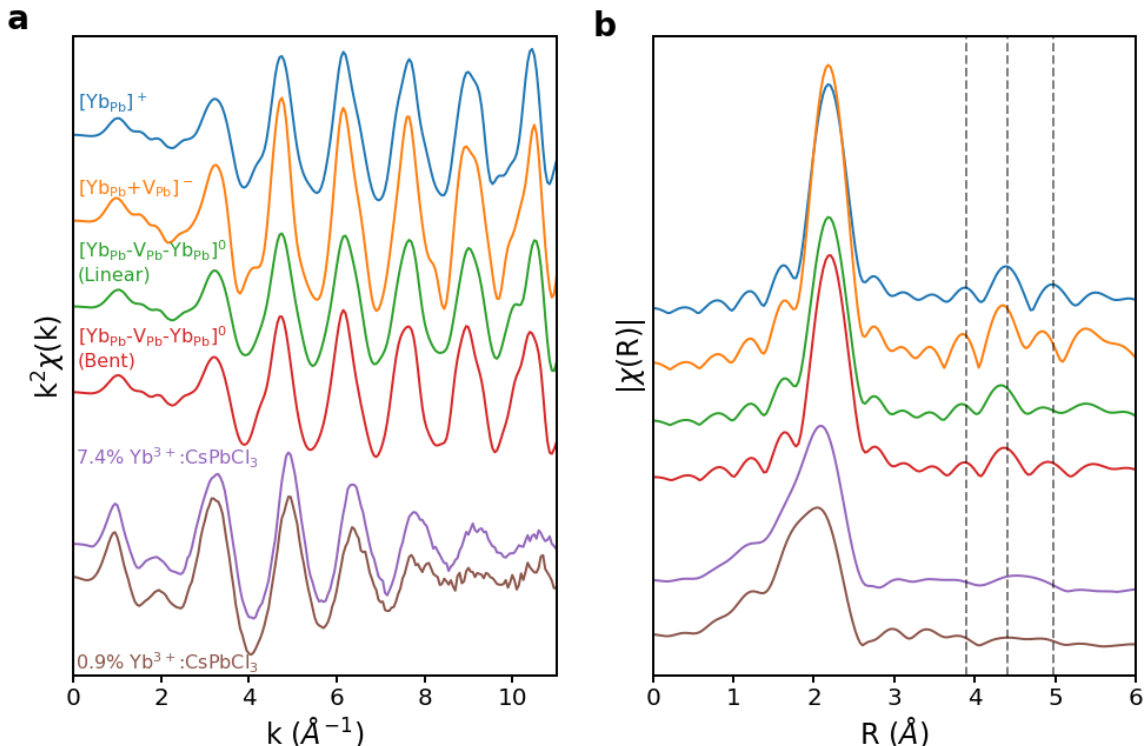


**Figure 4.** EXAFS spectra calculated from AIMD trajectories (top) from each calculated structure of Fig. 3, compared with Yb  $L_{3}$ -edge EXAFS data (purple, brown) in **(a)**  $k$ -space and **(b)**  $R$ -space for 7.4%- and 0.9%-doped  $\text{Yb}^{3+}:\text{CsPbCl}_3$  single crystals. Dashed lines in **(b)** serve as a guide for the eye on minor peak positions.

**PDF Characterization.** Figure 5a shows PDF profiles ( $G(r)$ ) measured from powders of the same  $\text{CsPbCl}_3$ , 0.9%  $\text{Yb}^{3+}:\text{CsPbCl}_3$ , and 7.4%  $\text{Yb}^{3+}:\text{CsPbCl}_3$  samples used above. All three curves are qualitatively similar to those previously reported for undoped  $\text{CsPbBr}_3$  perovskites, [22,23] with the expected reduction in  $G(r)$  intensity due to the use here of  $\text{Cl}^-$  rather than the more electron-rich  $\text{Br}^-$ . PDF calculations based on existing crystal structures [35] predict the short-range peaks associated with specific atom pairs: Pb-Cl, Cs-Cl, Pb-Cs, and Pb-Pb (Figure 5). The Cs-associated peaks, particularly the Cs-Cl atom pair, show large broadening as expected from the distribution of Cs bond distances in this host lattice [35]. Although the overall PDF

results are very similar for all three samples, subtle differences are apparent, particularly in the 7.4%  $\text{Yb}^{3+}:\text{CsPbCl}_3$  data. Notable features include a shoulder on the Pb-Cl peak at  $\sim 2.58 \text{ \AA}$  and reductions in the peak intensities marked with green and black dashed lines in Figure 5. To highlight these differences, Figure 5b shows differential PDF (dPDF,  $D(r)$ ) data obtained by subtracting the  $\text{CsPbCl}_3$  data from the  $\text{Yb}^{3+}:\text{CsPbCl}_3$  data. The 0.9% data in Figure 5b are magnified by a factor of 8 to facilitate comparison with the 7.4% data. These dPDF data reveal a clear increase in intensity of the shoulder near the Pb-Cl peak, as well as negative intensities marked with the black dashed lines. The 0.9% data appear to share the same features as the 7.4% data except with smaller amplitudes and hence lower signal-to-noise ratios. Partial PDF calculations show that the majority of these negative  $D(r)$  intensities correspond to Pb-Pb atom pairs (black dashed lines in Figure 5, see Figure S7 in Supplemental Material [24]). These results demonstrate a loss of Pb-Pb atom pair correlation upon  $\text{Yb}^{3+}$  doping in  $\text{CsPbCl}_3$ .

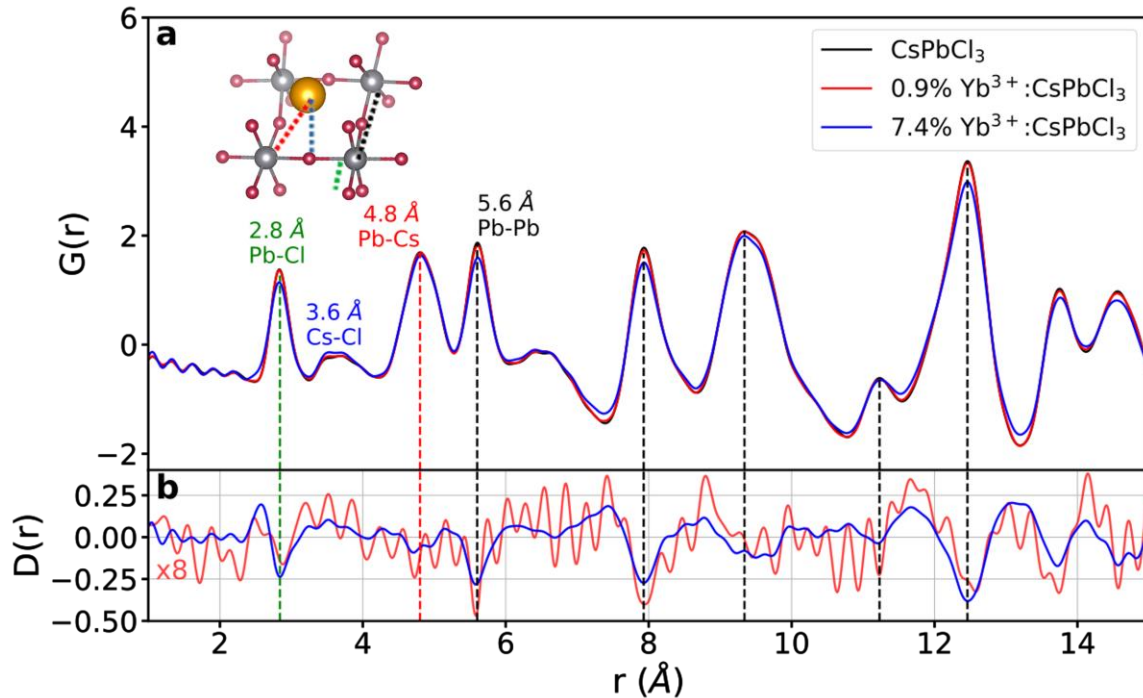


**Figure 5.** (a) Experimental Pair Distribution Function profiles (PDF,  $G(r)$ ) measured for  $\text{CsPbCl}_3$ , 0.9%  $\text{Yb}^{3+}:\text{CsPbCl}_3$ , and 7.4%  $\text{Yb}^{3+}:\text{CsPbCl}_3$  powdered single crystals. Primary short-range-order peaks are labeled. Inset: color-coordinated illustration of key atom pairs in the  $\text{CsPbCl}_3$  structure. Black dashed lines denote peaks with significant Pb-Pb pair contribution, the green dashed line denotes the Pb-Cl pair peak, and the red dashed line the Pb-Cs pair peak. (b) Differential PDFs (dPDF,  $D(r)$ ) obtained by subtracting the  $\text{CsPbCl}_3$  PDF from the PDFs of each of the  $\text{Yb}^{3+}$ -doped samples. Note that the 0.9%  $\text{Yb}^{3+}:\text{CsPbCl}_3$   $D(r)$  amplitudes are multiplied by 8x to allow representation on the same y

scale as the 7.4%  $\text{Yb}^{3+}:\text{CsPbCl}_3$  data.

Figure 6 enlarges the PDF and dPDF data for the 7.4%  $\text{Yb}^{3+}:\text{CsPbCl}_3$  sample from Figure 5 between 2.3 and 3.2 Å to focus on just the first M-Cl feature. These data highlight the appearance of a shoulder on the left side of the Pb-Cl peak upon  $\text{Yb}^{3+}$  doping, at  $r = 2.58$  Å. This shoulder coincides with a corresponding decrease in the Pb-Cl peak intensity. No similar shoulder is observed at higher  $r$  values. The location of this peak is consistent with the  $r = 2.6$  Å Yb-Cl nearest-neighbor distance observed by EXAFS (Figure 2). We thus assign the shoulder at 2.58 Å to Yb-Cl pairs. This distance is slightly shorter than those calculated by DFT for the model system of gas-phase  $\text{YbCl}_6^{3-}$  (2.680 Å), [44] and those predicted by ground state DFT for Yb-Cl in  $\text{CsPbCl}_3$  (2.62 Å) [12]. For comparison, the red and green markers in Figure 6 show the peak values of  $G(r)$  and  $D(r)$  predicted from PDF simulations based on DFT-calculated defect structures (*vide infra*).

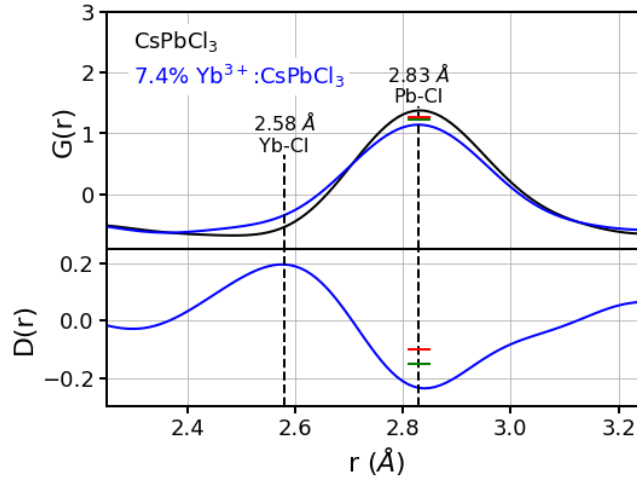


**Figure 6.** Pb-Cl peak region in the PDF of  $\text{CsPbCl}_3$  (black) and 7.4%  $\text{Yb}^{3+}:\text{CsPbCl}_3$  (blue) and dPDF of 7.4%  $\text{Yb}^{3+}:\text{CsPbCl}_3$  powdered single crystals. The 7.4%  $\text{Yb}^{3+}:\text{CsPbCl}_3$  data show a decrease in the Pb-Cl peak intensity at 2.8 Å and an increase in intensity at  $\sim 2.57$  Å, consistent with the loss of  $\text{Pb}^{2+}-\text{Cl}^-$  bonds and the appearance of  $\text{Yb}^{3+}-\text{Cl}^-$  bonds. A similar result is obtained for the 0.9%  $\text{Yb}^{3+}:\text{CsPbCl}_3$  data, but with a diminished signal-to-noise ratio (Figure 5b). Red markers indicate predicted changes in the peak intensity for  $\text{Yb}^{3+}$  substitution without any  $\text{Pb}^{2+}$  vacancies, and green markers indicate predicted changes with 0.5  $\text{Pb}^{2+}$  vacancies per  $\text{Yb}^{3+}$ .

Figure 7 compares the experimental dPDF data for the 7.4%  $\text{Yb}^{3+}:\text{CsPbCl}_3$  sample with dPDFs calculated from each of the AIMD-computed defect structures shown in Figure 3. Additionally, two non-local defect scenarios were considered, represented by the sum of two

$[\text{Yb}_{\text{Pb}}]^+$  with one  $[\text{V}_{\text{Pb}}]^{2-}$  and the sum of one  $[\text{Yb}_{\text{Pb}}-\text{V}_{\text{Pb}}]^-$  site with one  $[\text{Yb}_{\text{Pb}}]^+$ .  $D(r)$  profiles were calculated from 1 ps AIMD trajectories run on the various DFT-optimized structures. No difference was observed between the calculated PDFs of the linear vs orthogonal  $[\text{Yb}_{\text{Pb}}-\text{V}_{\text{Pb}}-\text{Yb}_{\text{Pb}}]^0$  arrangements, so the orthogonal was arbitrarily chosen to be shown in these results. Significant features in the data are marked with vertical dashed lines. In general, all simulations give reasonable representations of the data (Figure S12, Supplemental Material [24]), reproducing the positions, heights, and peak shapes for the majority of the features. The simulations consistently show a significant decrease of the Cs-Pb distance upon doping, however, whereas the data show a slight increase. This difference is likely due to lattice distortions around the  $\text{Cs}^+$  sites, as observed in our DFT calculations [12]. Computational work [12] predicted, for a Yb concentration of 7.4%, 95% of  $\text{Yb}_{\text{Pb}}$  dopants to be within one exciton Bohr radius of a compensating  $\text{V}_{\text{Pb}}$  defect, for example, in the  $[\text{Yb}_{\text{Pb}}-\text{V}_{\text{Pb}}-\text{Yb}_{\text{Pb}}]^0$  arrangement shown here. Qualitatively, the  $[\text{Yb}_{\text{Pb}}-\text{V}_{\text{Pb}}-\text{Yb}_{\text{Pb}}]^0$  simulation is most similar to the experimental data, particularly around the Pb-Cl peak. A reduced  $\chi^2$  and r-squared goodness-of-fit analysis (not shown) shows statistically similar results for all structures, however, preventing quantitative discrimination between proposed defect structures. This goodness-of-fit is primarily compromised by the difference between experimental and computed distortions of the  $\text{Cs}^+$  sublattice upon  $\text{Yb}^{3+}$  doping, which hinders statistical comparisons in the other regions of interest as well.

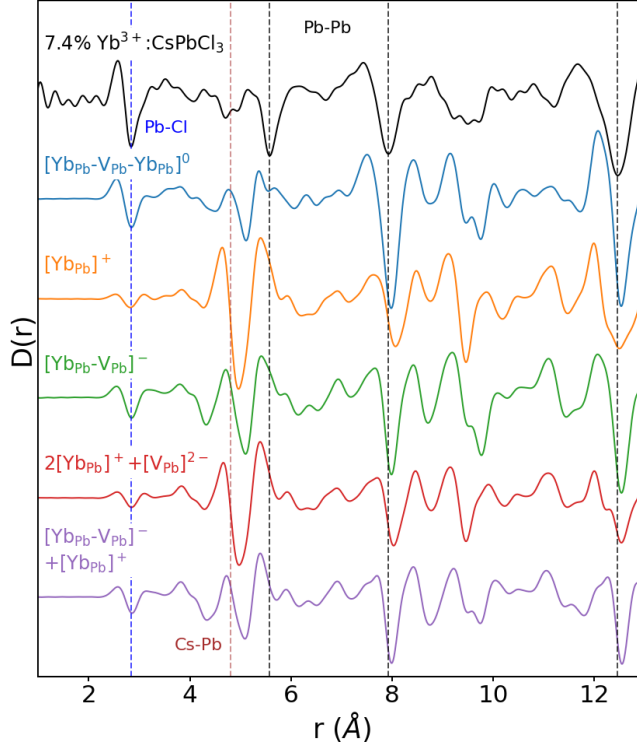


**Figure 7.** Comparison of the experimental differential PDF (dPDF) for 7.4%  $\text{Yb}^{3+}:\text{CsPbCl}_3$  (black) with simulated dPDFs for the various calculated defect structures depicted in Figure 3. The bent dimer simulation was arbitrarily chosen for  $[\text{Yb}_{\text{Pb}}-\text{V}_{\text{Pb}}-\text{Yb}_{\text{Pb}}]^0$ . Two additional dPDFs included to account for non-local charge compensation ( $2[\text{Yb}_{\text{Pb}}]^+ + [\text{V}_{\text{Pb}}]^{2-}$ , and  $[\text{Yb}_{\text{Pb}}-\text{V}_{\text{Pb}}]^- + [\text{Yb}_{\text{Pb}}]^+$ ) were obtained by averaging the PDFs of their specified components. The Pb-Cl peak has been marked with a blue dashed line, and several Pb-Pb peaks are marked with black dashed lines. The position of the Cs-Pb peak in the data, poorly reproduced by the simulations, is marked with a brown dashed line.

To compare with the experimental data in Figure 5, we also calculated the percent changes in peak intensities (relative to an undoped sample) anticipated from the simulated PDF data for the Pb-Cl, Pb-Cs, and Pb-Pb peaks in the short-range-order region of the data. These results are summarized in Table I along with the parallel experimental intensity changes, and are illustrated graphically in Figure 6 for the Pb-Cl bond distance of the 7.4%  $\text{Yb}^{3+}:\text{CsPbCl}_3$  sample. The Cs-Cl peak was not analyzed due to its breadth and lack of a clear maximum. The selected peaks, marked in Figure 5, were chosen to allow quantitative analysis of  $\text{Pb}^{2+}$  vacancy formation upon  $\text{Yb}^{3+}$  doping. Although inhomogeneous peak broadening can also decrease peak intensities, peak broadening here results primarily from  $\text{Yb}^{3+}$  doping and  $\text{Pb}^{2+}$  vacancy formation (Figure 7), thus allowing us to correlate intensity changes with the presence of  $\text{Yb}_{\text{Pb}}$  and  $\text{V}_{\text{Pb}}$  defects. Expected changes in peak intensities, based on the experimental  $\text{Yb}^{3+}$  doping levels, are



tabulated for the two cases of no  $\text{Pb}^{2+}$  vacancies (No  $V_{\text{Pb}}$ ) and 0.5  $\text{Pb}^{2+}$  vacancies per  $\text{Yb}^{3+}$  ( $V_{\text{Pb}}$ ), the latter being the expected value for charge neutrality. Critically,  $V_{\text{Pb}}$  formation is evident from all three Pb-related short-range peaks of both doped samples. Because all three peaks are in the short-range order regime, these changes do not involve contributions from other atom pairs. We therefore conclude that  $\text{Yb}^{3+}$  doping is accompanied by the formation of  $\text{Pb}^{2+}$  vacancies in  $\text{CsPbCl}_3$ . Although widely hypothesized and computationally predicted, these data are the first to demonstrate this key structural finding for lanthanide-doped lead-halide perovskites.

**Table I.** Predicted and experimental percent changes in the intensities of select short-range order peaks in the PDF data (as marked in Figure 5) resulting from  $\text{Yb}^{3+}$  doping. Predicted changes are given for the cases of (i) no  $\text{Pb}^{2+}$  vacancies (No  $V_{\text{Pb}}$ ) and (ii) 0.5  $V_{\text{Pb}}$  per  $\text{Yb}^{3+}$  dopant ( $V_{\text{Pb}}$ ). The changes observed experimentally are also tabulated. Experimental uncertainties are 0.13 for 0.9% data and 0.12 for 7.4% data.

	$r$ (Å)	0.9% $\text{Yb}^{3+}:\text{CsPbCl}_3$			7.4% $\text{Yb}^{3+}:\text{CsPbCl}_3$		
		Predicted		Obsd.	Predicted		Obsd.
		No $V_{\text{Pb}}$	$V_{\text{Pb}}$		No $V_{\text{Pb}}$	$V_{\text{Pb}}$	
Pb-Cl	2.83	-0.9	-1.4	-1.2	-7.4	-11.1	-17.0
Pb-Cs	4.80	-0.0	-0.5	-0.8	-0.1	-3.8	-3.6
Pb-Pb	5.60	-0.2	-1.1	-3.0	-1.7	-9.1	-14.9

Although the PDF data show  $V_{\text{Pb}}$  formation as the primary charge-compensation mechanism accompanying  $\text{Yb}^{3+}$  doping, we note that they also appear to show slightly greater peak intensity changes than anticipated for the precise scenario of 0.5  $\text{Pb}^{2+}$  vacancies per  $\text{Yb}^{3+}$  (see Table I). Each peak yields a different quantitative value, but averaging over the results for all three peaks indicates  $0.9 \pm 0.6 V_{\text{Pb}}/\text{Yb}^{3+}$  in the 0.9%  $\text{Yb}^{3+}:\text{CsPbCl}_3$  sample and  $0.9 \pm 0.4 V_{\text{Pb}}/\text{Yb}^{3+}$  in the 7.4%  $\text{Yb}^{3+}:\text{CsPbCl}_3$  sample, for example. Graphically, Figure 6 shows that the experimental change in Pb-Cl peak intensity exceeds that predicted for a ratio of 0.5  $V_{\text{Pb}}/\text{Yb}^{3+}$ . Such discrepancies could stem from the inability to accurately quantify integrated peak intensities in the PDF data, but in Figure 6 we see little evidence of Pb-Cl peak broadening that is not accounted for by the appearance of the neighboring Yb-Cl peak. It is unclear why excess lattice  $\text{Pb}^{2+}$  vacancies beyond those required for  $\text{Yb}^{3+}$  charge compensation might form upon  $\text{Yb}^{3+}$  doping, but there may be other sources of disorder induced by  $\text{Yb}^{3+}$  doping as well. For example, we observe a reduction in macroscopic single-crystal quality with increasing  $\text{Yb}^{3+}$  doping that could reflect increased densities of twinning grain boundaries (*e.g.*, Figure S1).



Nevertheless, the average peak-intensity change still falls within experimental uncertainty of that anticipated for  $0.5 V_{\text{Pb}}/\text{Yb}^{3+}$ , and is consistent with our conclusion that  $V_{\text{Pb}}$  formation is the primary mode of  $\text{Yb}^{3+}$  charge compensation.

## Conclusion

A combination of XRD, EXAFS, and PDF data and analysis have been used to measure the structural consequences of doping  $\text{Yb}^{3+}$  ions into perovskite  $\text{CsPbCl}_3$  crystal lattices. The results show that ytterbium is incorporated into  $\text{CsPbCl}_3$  in its 3+ oxidation state, substituting exclusively at  $\text{Pb}^{2+}$  sites, and adopting a pseudo-octahedral  $\text{Cl}^-$  coordination environment similar to that of  $\text{Pb}^{2+}$  but with contracted bond lengths. EXAFS and PDF measurements both show  $\text{Yb}^{3+}\text{-Cl}^-$  bond lengths of 2.58 Å, compared to the  $\text{Pb}^{2+}\text{-Cl}^-$  distances of 2.83 Å. The PDF data also show evidence of extensive  $\text{Pb}^{2+}$  vacancy formation upon  $\text{Yb}^{3+}$  doping, indicating this as the primary mechanism for compensation of the excess positive charges of  $\text{Yb}^{3+}$  dopants. These conclusions are bolstered by comparison of dPDF data with simulations. As such, the results of this study represent the first experimental evidence of correlated  $\text{Yb}^{3+}$  doping and  $\text{Pb}^{2+}$  vacancy formation in  $\text{Yb}^{3+}$ -doped  $\text{CsPbCl}_3$ , a motif that has been frequently hypothesized but never observed, and that is believed to play an important mechanistic role in the unique quantum cutting displayed by this material. Overall, this work advances our basic structural understanding of lanthanide-doped lead-halide perovskites in ways that will help to develop a deeper understanding of structure/function relationships in this class of materials, from lattice stabilization to quantum cutting.

**Acknowledgments.** This research was primarily supported by the UW Molecular Engineering Materials Center, an NSF Materials Research Science and Engineering Center (Grant No. DMR-1719797). This research used resources of the Advanced Photon Source, a U.S. Department of Energy (DOE) Office of Science User Facility operated for the DOE Office of Science by Argonne National Laboratory under Contract No. DE-AC02-06CH11357. We acknowledge Steve Heald from APS Sector 20 (BL 20-ID) (GUPs 69365, 73609, & 74833) and Olaf Borkiewicz and Leighanne Gallington from Sector 11 (BL 11-ID) (GUP 73957) for collecting these data sets. We also thank Micah P. Prange for his assistance with EXAFS theory and calculations and Reinhard Neder for assistance using DISCUS.

## References

- [1] Y. Zhou, J. Chen, O. M. Bakr, and H.-T. Sun, *Chem. Mater.* **30**, 6589 (2018).
- [2] J. Shi, F. Li, J. Yuan, X. Ling, S. Zhou, Y. Qian, and W. Ma, *J. Matter. Chem. A* **7**, 20936 (2019).
- [3] D. Zhou, R. Sun, W. Xu, N. Ding, D. Li, X. Chen, G. Pan, X. Bai, and H. Song, *Nano Lett.* **19**, 6904 (2019).
- [4] W. J. Mir, T. Sheikh, H. Arfin, Z. Xia, and A. Nag, *NPG Asia Mater.* **12**, 9 (2020).
- [5] S. M. Ferro, M. Wobben, and B. Ehrler, *Mater. Horiz.* **8**, 1072 (2021).
- [6] D. Zhou, D. Liu, G. Pan, X. Chen, D. Li, W. Xu, X. Bai, and H. Song, *Adv. Mater.* **29**, 1704149 (2017).
- [7] G. Pan, X. Bai, D. Yang, X. Chen, P. Jing, S. Qu, L. Zhang, D. Zhou, J. Zhu, W. Xu, B. Dong, and H. Song, *Nano Lett.* **17**, 8005 (2017).
- [8] T. J. Milstein, D. M. Kroupa, and D. R. Gamelin, *Nano Lett.* **18**, 3792 (2018).
- [9] T. J. Milstein, K. T. Kluherz, D. M. Kroupa, C. S. Erickson, J. J. De Yoreo, and D. R. Gamelin, *Nano Lett.* **19**, 1931 (2019).
- [10] M. J. Crane, D. M. Kroupa, and D. R. Gamelin, *Energy Environ. Sci.* **12**, 2486 (2019).
- [11] J. Y. D. Roh, M. D. Smith, M. J. Crane, D. Biner, T. J. Milstein, K. W. Krämer, and D. R. Gamelin, *Phys. Rev. Mater.* **4**, 105405 (2020).
- [12] D. E. Sommer, D. R. Gamelin, and S. T. Dunham, *Phys. Rev. Mater.* **6**, 025404 (2022).
- [13] T. J. Milstein, J. Y. D. Roh, L. M. Jacoby, M. J. Crane, D. E. Sommer, S. T. Dunham, and D. R. Gamelin, *Chem. Mater.* **34**, 3759 (2022).
- [14] B. W. Bryant, *J. Opt. Soc. Am.* **55**, 771 (1965).
- [15] M. Zeng, F. Artizzu, J. Liu, S. Singh, F. Locardi, D. Mara, Z. Hens, and R. Van Deun, *ACS Appl. Nano Mater.* **3**, 4699 (2020).
- [16] W. J. Chang, S. Irgen-Gioro, S. Padgaonkar, R. López-Arteaga, and E. A. Weiss, *J. Phys. Chem. C* **125**, 25634 (2021).
- [17] M. Stefanski, V. Boiko, M. Ptak, and W. Streck, *J. Alloys Compounds* **905**, 164216 (2022).
- [18] Z.-J. Yong, S.-Q. Guo, J.-P. Ma, J.-Y. Zhang, Z.-Y. Li, Y.-M. Chen, B.-B. Zhang, Y. Zhou, J. Shu, J.-L. Gu, L.-R. Zheng, O. M. Bakr, and H.-T. Sun, *J. Am. Chem. Soc.* **140**, 9942 (2018).
- [19] J.-P. Ma, Y.-M. Chen, L.-M. Zhang, S.-Q. Guo, J.-D. Liu, H. Li, B.-J. Ye, Z.-Y. Li, Y. Zhou, B.-B. Zhang, O. M. Bakr, J.-Y. Zhang, and H.-T. Sun, *J. Matter. Chem. C* **7**, 3037 (2019).
- [20] J. Ma, Q. Yao, J. A. McLeod, L.-Y. Chang, C.-W. Pao, J. Chen, T.-K. Sham, and L. Liu, *Nanoscale* **11**, 6182 (2019).
- [21] C. Bi, S. Wang, Q. Li, S. V. Kershaw, J. Tian, and A. L. Rogach, *J. Phys. Chem. Lett.*, 943 (2019).
- [22] F. Bertolotti, L. Protesescu, M. V. Kovalenko, S. Yakunin, A. Cervellino, S. J. L. L. Billinge, M. W. Terban, J. S. Pedersen, N. Masciocchi, and A. Guagliardi, *ACS Nano* **11**, 3819 (2017).
- [23] P. Cottingham, and R. L. Brutchey, *Chem. Mater.* **30**, 6711 (2018).
- [24] See Supplemental Material at [URL will be inserted by publisher] for additional characterization figures and tables of EXAFS fitting parameters.
- [25] M. J. Crane, D. M. Kroupa, J. Y. Roh, R. T. Anderson, M. D. Smith, and D. R. Gamelin, *ACS Appl. Energy Mater.* **2**, 4560 (2019).

- [26] B. Ravel, and M. Newville, *J. Synch. Rad.* **12**, 537 (2005).
- [27] J. J. Rehr, and R. C. Albers, *Rev. Mod. Phys.* **72**, 621 (2000).
- [28] J. J. Rehr, J. J. Kas, M. P. Prange, A. P. Sorini, Y. Takimoto, and F. Vila, *Compt. Rend. Phys.* **10**, 548 (2009).
- [29] J. J. Rehr, J. J. Kas, F. D. Vila, M. P. Prange, and K. Jorissen, *Phys. Chem. Chem. Phys.* **12**, 5503 (2010).
- [30] A. Hoehner, S. Mergelsberg, O. J. Borkiewicz, P. M. Dove, and F. M. Michel, *Acta Cryst. Sect. A* **75**, 758 (2019).
- [31] B. H. Toby, and R. B. Von Dreele, *J. Appl. Cryst.* **46**, 544 (2013).
- [32] P. Juhás, T. Davis, C. L. Farrow, and S. J. L. Billinge, *J. Appl. Cryst.* **46**, 560 (2013).
- [33] X. Qiu, J. W. Thompson, and S. J. L. Billinge, *J. Appl. Cryst.* **37**, 678 (2004).
- [34] C. L. Farrow, P. Juhás, J. W. Liu, D. Bryndin, E. S. Božin, J. Bloch, T. Proffen, and S. J. L. Billinge, *J. Phys.: Cond. Matter* **19**, 335219 (2007).
- [35] M. R. Linaburg, E. T. McClure, J. D. Majher, and P. M. Woodward, *Chem. Mater.* **29**, 3507 (2017).
- [36] T. Proffen, and R. B. Neder, *J. Appl. Cryst.* **30**, 171 (1997).
- [37] G. Kresse, and J. Furthmüller, *Comp. Mater. Sci.* **6**, 15 (1996).
- [38] G. Kresse, and J. Furthmüller, *Phys. Rev. B* **54**, 11169 (1996).
- [39] P. E. Blöchl, *Phys. Rev. B* **50**, 17953 (1994).
- [40] J. P. Perdew, A. Ruzsinszky, G. I. Csonka, O. A. Vydrov, G. E. Scuseria, L. A. Constantin, X. Zhou, and K. Burke, *Phys. Rev. Lett.* **100**, 136406 (2008).
- [41] C. Freysoldt, B. Grabowski, T. Hickel, J. Neugebauer, G. Kresse, A. Janotti, and C. G. Van de Walle, *Rev. Mod. Phys.* **86**, 253 (2014).
- [42] H. J. Monkhorst, and J. D. Pack, *Phys. Rev. B* **13**, 5188 (1976).
- [43] J. A. McLeod, Z. Wu, B. Sun, and L. Liu, *Nanoscale* **8**, 6361 (2016).
- [44] M. Atanasov, C. Daul, H. U. Güdel, T. A. Wesolowski, and M. Zbiri, *Inorg. Chem.* **44**, 2954 (2005).